

Coupling of Electron Channeling with EBSD: Toward the Quantitative Characterization of Deformation Structures in the SEM

I. GUTIERREZ-URRUTIA,^{1,2} S. ZAEFFERER,¹ and D. RAABE¹

1.—Max-Planck-Institut für Eisenforschung, 40237 Dusseldorf, Germany. 2.—e-mail: i.gutierrez@mpie.de

The coupling of electron channeling contrast imaging (ECCI) with electron backscatter diffraction (EBSD) provides an efficient and fast approach to perform ECCI of crystal defects, such as dislocations, cells, and stacking faults, under controlled diffraction conditions with enhanced contrast. From a technical point of view, the ECCI technique complements two of the main electron microscopy techniques, namely, EBSD and conventional diffraction-based transmission electron microscopy. In this review, we provide several application examples of the EBSD-based ECCI approach on microstructure characterization, namely, characterization of single dislocations, measurement of dislocation densities, and characterization of dislocation substructures in deformed bulk materials. We make use of a two-beam Bloch wave approach to interpret the channeling contrast associated with crystal defects. The approach captures the main features observed in the experimental contrast associated with stacking faults and dislocations.

INTRODUCTION

The characterization of deformation substructures is commonly performed by transmission electron microscopy (TEM) techniques. The high spatial and angular resolution of TEM allows for the characterization of individual crystal defects such as dislocations, stacking faults, and point defects, as well as for more complex configurations formed by dislocations and deformation twins.^{1–3} However, TEM presents some drawbacks such as sample preparation, where extremely thin samples are needed, and reduced observation area. The common methods for TEM sample preparation, namely, electropolishing, ion milling, and focused ion beam (FIB), are time consuming and may even modify the microstructure by introducing point defects (for instance, foil thinning by ion milling⁴) or relaxing internal stresses (bulk thinning prior to electropolishing).⁵ Furthermore, the resulting TEM foil offers only a limited observation area ($\sim 100 \times 100 \mu\text{m}^2$), making it difficult to perform the quantitative microstructural characterization required by many topics in materials science. While TEM has proven to be a very versatile tool for the characterization of

crystal defects, the limitations outlined earlier have led to the development of diffraction-based methods such as x-ray diffraction (XRD),^{6,7} synchrotron radiation-based techniques,^{8–10} and 2D/3D electron backscatter diffraction (EBSD) techniques.^{11–15} An alternative electron microscopy technique for characterizing bulk deformed materials is electron channeling contrast imaging (ECCI).^{16–18} ECCI is a scanning electron microscope (SEM) technique that makes use of the strong dependence of the backscatter electron (BSE) signal on the orientation of the crystal lattice planes with respect to the incident electron beam due to the electron channeling mechanism. Interestingly, slight local distortions in the crystal lattice produced by the strain fields associated with dislocations yield a modulation in the BSE signal that can be detected by available BSE detectors. Accordingly, crystal defects such as dislocations can be imaged by ECCI in the SEM. According to the dynamical theory of electron diffraction, the optimum diffraction contrast for imaging crystal defects in ECCI is obtained by orienting the crystal exactly into Bragg condition for a selected set of diffracting lattice planes.¹⁹ However, since the early observations in 1967 by Coates of

Kikuchi-like reflection patterns in the SEM, the so-called electron channeling patterns (ECPs),²⁰ the impact of ECCI in materials science has been rather limited. This is due to the specific tilting conditions required to image crystal defects in ECCI.

To date, two main ECCI setups have been developed, namely, forward-scatter electron (FSE) and BSE methods. FSE-based approaches make use of high-tilt, EBSD-type geometries to enhance the intensity of thermally diffuse (or phonon) scattered electrons. The FSE detector records the contrast created by the Kikuchi bands intersecting the detector. This configuration, originally used by Czernuszka et al.²¹ to image dislocations in Si and Ni₃Ga, has been adapted by Wilkinson's group^{16,22,23} and by Picard et al.^{24–26} to examine dislocations in SiGe/Si epitaxial layers²² and GaN and SiC thin films.^{23–26} BSE-based methods make use of electron channeling patterns to optimize the diffraction contrast of the crystal defect image. These patterns can be obtained after running the microscope at low magnification (so-called electron channeling patterns, ECPs)^{17,18,20} or after rocking the incoming beam on the material surface by a deflection focusing technique (so-called selected-area channeling patterns, SACPs).^{27–29} The main limitation of these approaches is the large observation area, typically >10 μm, and the low spatial resolution, 2 μm–5 μm. This shortcoming limits the application of ECPs/SACPs-based ECCI setups to lightly deformed coarse polycrystals and single crystals.^{16,29–32} Recently, we have proposed the use of EBSD to obtain the rocking parameters of the sample surface under the incoming beam (tilt and rotation angles) where the crystal is oriented into optimum diffraction contrast.³³ Due to the high spatial resolution of EBSD (35 ± 5 nm³⁴), crystal defects can be imaged in submicrometer areas of deformed bulk materials. In the last few years, we have applied the EBSD-based ECCI approach to several cases, namely, the characterization of complex deformation structures such as dislocation and nano-twin substructures in bulk deformed high-Mn TWIP steels (TWIP: twinning induced plasticity),^{35–39} the investigation of dislocation patterns,^{36,37,40} the measurement of dislocation densities in deformed alloys,^{41,42} and the characterization of individual dislocations and stacking faults.^{43,44} These studies have demonstrated the feasibility of the EBSD-based ECCI approach on the quantitative characterization of complex deformation structures in bulk materials. From a technical point of view, the ECCI technique complements two of the main electron microscopy techniques, namely, EBSD and conventional diffraction-based TEM. The present paper summarizes the experimental configuration of the EBSD-based ECCI setup and illustrates its use with several experimental studies. We also provide a physical-based model of electron channeling contrast associated with crystals defects.

EXPERIMENTAL CONFIGURATION

The EBSD-based ECCI observations were carried out with a Cross Beam XB 1540 FIB instrument (Carl Zeiss SMT AG, Germany) consisting of a Gemini-type field emission gun (FEG) electron column combined with a FIB device (Orsay Physics). This instrument is equipped with a TSL OIM EBSD system. EBSD maps were measured at 15 kV acceleration voltage and a working distance of 15 mm. ECCI was conducted at acceleration voltages between 10 kV and 30 kV, using a solid-state, four-quadrant BSE detector. Working distances of 5 mm–7 mm were used with sample tilts ranging from –10° to 30°. The microscope was run in the “high current” mode, and an objective lens aperture of 120 μm was used. The experimental electron beam parameters were the following: electron beam, 7 nA–10 nA; half-beam convergence angle, 5 mrad–6 mrad; and spatial resolution, 3 nm–3.5 nm.

Figure 1 shows a sketch of the EBSD-based ECCI setup. This setup is made up of two sample configurations, namely, ECCI position (a) and EBSD position (b). In the ECCI configuration, the sample surface is positioned perpendicular to the incident electron beam. The initial settings are 0° tilt/rotation angles. In the EBSD position, the sample is tilted 20° from the incident electron beam using a conventional EBSD geometry.¹⁶ We have selected a low-tilt ECCI configuration, originally introduced by Crimp's group,^{31,45} instead of a high-tilt, EBSD-type configuration because of the convenient position for performing crystal orientation experiments (i.e., tilt and rotation experiments), the higher spatial resolution (~10 nm against ~50 nm⁴³), the enhanced electron channeling contrast (~10 mrad against ~160 mrad⁴³), and the isotropic interaction volume. In the high-tilt, EBSD-type configuration, the interaction volume is anisotropic leading to a significantly lower lateral resolution in the direction along the surface perpendicular to the tilt axis.

The operation mode of the EBSD-based ECCI setup is as follows: First, EBSD scans are performed on sample areas previously selected by ECCI at the low-tilt configuration. Electron channeling patterns are thereafter calculated from the crystal orientation determined by EBSD by means of computer software^{43,46} (Fig. 1c). The simulations were performed using a kinematical approach except those involving the width and intensity of Kikuchi bands, where a two-beam dynamical approach was instead applied.⁴³ This code also calculates the tilt and rotation angles required to obtain the ECC image of a crystal defect under two-beam diffraction conditions for one well-defined set of lattice planes. This diffraction condition is obtained after superimposing the primary beam direction on one of the simulated Kikuchi lines far out of any principal zone axis. Subsequently, the microscope stage is positioned according to these predetermined tilt and

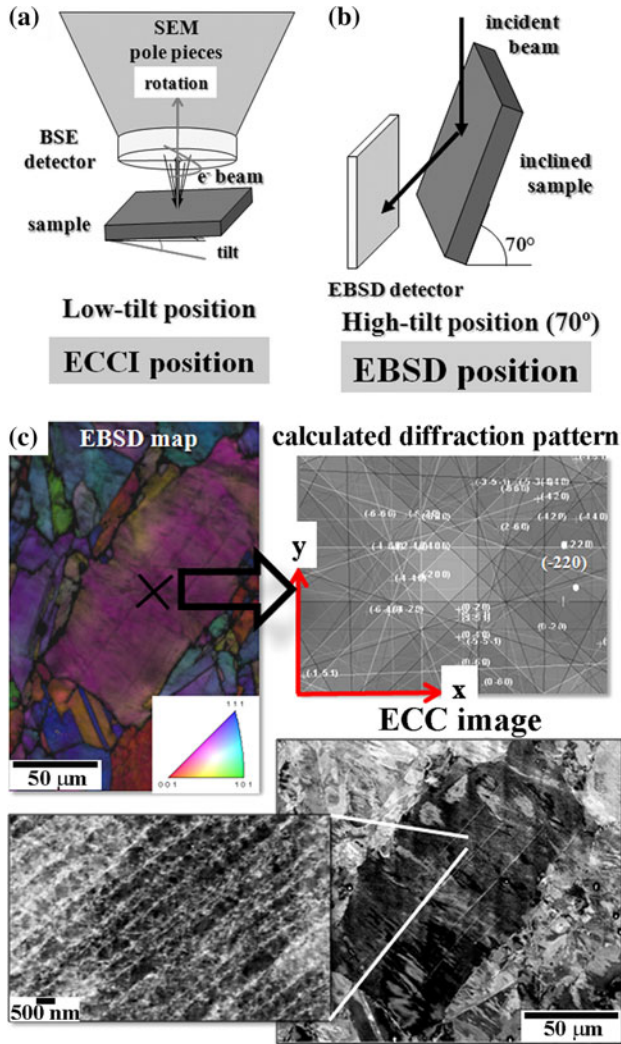


Fig. 1. (a–b): Sketch of the EBSD-based ECCI configuration. The setup is made up of two sample configurations, namely, low-tilt ECCI position (a) and EBSD position (b). (c): Illustration of the operation mode of the ECCI setup to perform ECCI under controlled diffraction conditions.

rotation angles, and the ECC image of the selected area at optimum contrast is attained.

THEORETICAL BACKGROUND

Electron Scattering Mechanisms Related to Electron Channeling

The most relevant scattering mechanisms involved in the formation of electron channeling contrast are the following: Bragg scattering, core-loss scattering, and multiple scattering.^{43,47} Bragg scattering is an elastic and coherent scattering event that has a large cross section for small scattering angles in the order of few degrees. Bragg scattering is the mechanism that leads to the formation of Bloch wave fields and, consequently, to conventional Bragg diffraction. Core-loss scattering processes correspond to inelastic scattering events

involving large energy losses (between 10 eV and 10 keV) and very small scattering angles. These scattering processes lead to the formation of electromagnetic radiation (x-rays, light), plasmons, or secondary electrons.⁴⁸ Finally, and very important for backscattering, inelastic and phonon scattering events combine to a chain of scattering events comprised as multiple scattering. This is characterized by large scattering angles and a wide energy distribution of electrons. Multiple scattering is commonly considered the main scattering event in the calculation of the spatial and spectral energy distribution of backscattered electrons in Monte-Carlo electron trajectory simulation programs.⁴⁹

The formation of the channeling contrast can be understood as follows:⁴³ The primary beam electrons that interact with the surface crystal are coherently (Bragg) scattered by the atoms of the crystal lattice and form a lattice-coherent electron wave. Depending on the orientation of the crystal lattice with respect to the primary electron beam direction, the coherent electron field contains density maxima at atom positions or further away, resulting in a different number of inelastic scattering events by core-loss scattering. The resulting low-energy electrons may, by multiple scattering, eventually leave the sample and be recorded as backscattered electrons with a broad energy distribution but with an orientation-dependent intensity.

Electron Channeling Contrast Associated with Lattice Defects

The electron channeling contrast associated with crystalline defects has been simulated by different approaches, namely, the numerical integration of two-beam Howie–Whelan equations⁵⁰ and Bloch wave-based models.^{19,51,52} Recently, we have made use of a two-beam Bloch wave approach that captures the main features observed in the experimental contrast associated with stacking faults and dislocations.⁴³ In this model, the orientation contribution to the total backscatter intensity can be written as:^{43,48}

$$\Delta\eta = \frac{N\sigma_B}{2\pi} \zeta'_0 \left(-\frac{(w + \zeta'_0/\zeta'_g)}{1 + w^2 - (\zeta'_0/\zeta'_g)^2} + \frac{w}{1 + w^2 + [(1 + w)(\zeta'_0/\zeta'_g)^2]} \right) \quad (1)$$

where N is the number of atoms per unit volume, σ_B is the cross section for backscattering, and $w = s \cdot \zeta_g$ with ζ_g being the extinction distance and s the excitation error that indicates the angular deviation of the primary electron beam wave vector, k_0 , from the exact Bragg position of the lattice planes with reciprocal lattice vector g . As example, we have

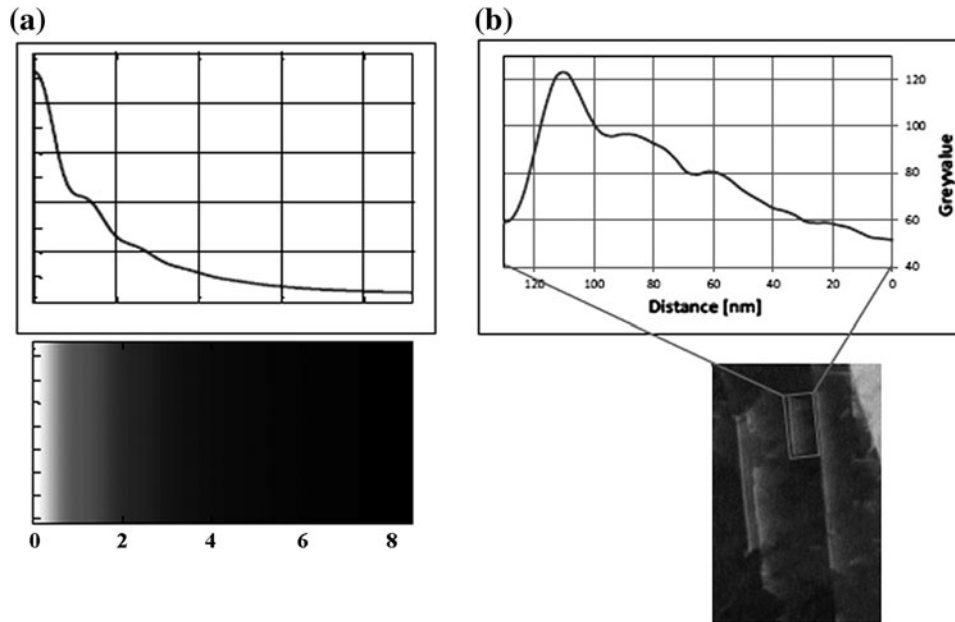


Fig. 2. Comparison of calculated (a) and experimental electron channeling contrast of a stacking fault. The calculation was performed by means of a two-beam Bloch wave approach. The experimental image was taken from a stacking fault in a high-Mn steel, observed under $g = (111)$ (g : diffraction vector).⁴³

calculated the backscattering intensity associated with a stacking fault (SF) laying in a depth z_{SF} below the surface (Fig. 2a).⁴³ In this calculation, we have assumed that the atoms below the SF are shifted by exactly half an atomic plane distance. This figure reveals that the intensity is highest close to the surface, which is associated with the intersection of the SF with the sample surface. The intensity profile is subsequently attenuated with characteristic but weak oscillations. The frequency of these oscillations, measured with respect to the distance, z , to the entry surface, corresponds to the effective extinction distances obtained under the current electron beam conditions, ξ_g^{eff} . Figure 2b shows an ECC image of a stacking fault in a high-Mn steel. The oscillations are well visible. From the number of oscillations, it is therefore possible to estimate the observation depth of crystal defects: For $g = (111)$, $E = 20$ keV, and an fcc-iron crystal structure, it yields $\xi_g = 13$ nm. In Fig. 2b, three bright lines are visible. Accordingly, the total visibility of the stacking fault is about five times this value, ~ 60 nm–70 nm. Interestingly, similar probe depths have been estimated from theoretical approaches in Fe alloys.⁴²

APPLICATION EXAMPLES OF ECCI TO THE CHARACTERIZATION OF DEFORMATION STRUCTURES

In recent years, we have successfully applied the EBSD-based ECCI approach to the characterization of several microstructural features, namely, single dislocations and stacking faults,^{42,43} nanotwins,^{35–37,43} and complex dislocation configurations,

such as cells, cell blocks, Taylor lattices, and microbands.^{35–38,40} It has been also proved as a valuable technique to measure dislocation densities.^{41–43} Figure 3 illustrates several application examples of the ECCI technique (details can be found in Refs. 40,41,43). In this section, we provide further details of two particular application examples, namely, the characterization of single dislocations and dislocation substructures.

Characterization of Single Dislocations

Single dislocations can be clearly imaged by ECCI at suitable diffraction conditions. ECC images of dislocations correspond to projected dislocation lines within the interaction probe depth, typically < 100 nm. The optimum dislocation contrast is attained by orienting the crystal into the channeling condition, which is close to the exact Bragg condition but with a small negative value of w (Eq. 1).^{19,43} In this diffraction condition, dislocations appear as bright lines on a dark background. Dislocation contrast becomes weaker when deviating from the exact channeling conditions. Figure 4a illustrates, as an example, an ECC image of dislocations taken after orienting the crystal into Bragg condition in a lightly deformed FeSi alloy with bcc crystal structure.⁴³ Three different dislocation sets are visible labeled as (i)–(iii). Two of them, namely, (i) and (ii), appear as straight long lines. Assuming that long dislocation segments in bcc structures usually contain a screw character with a $\langle 111 \rangle$ -type Burgers vector, we can index the corresponding Burgers vectors and line directions, provided that their inclination angles with respect to the surface

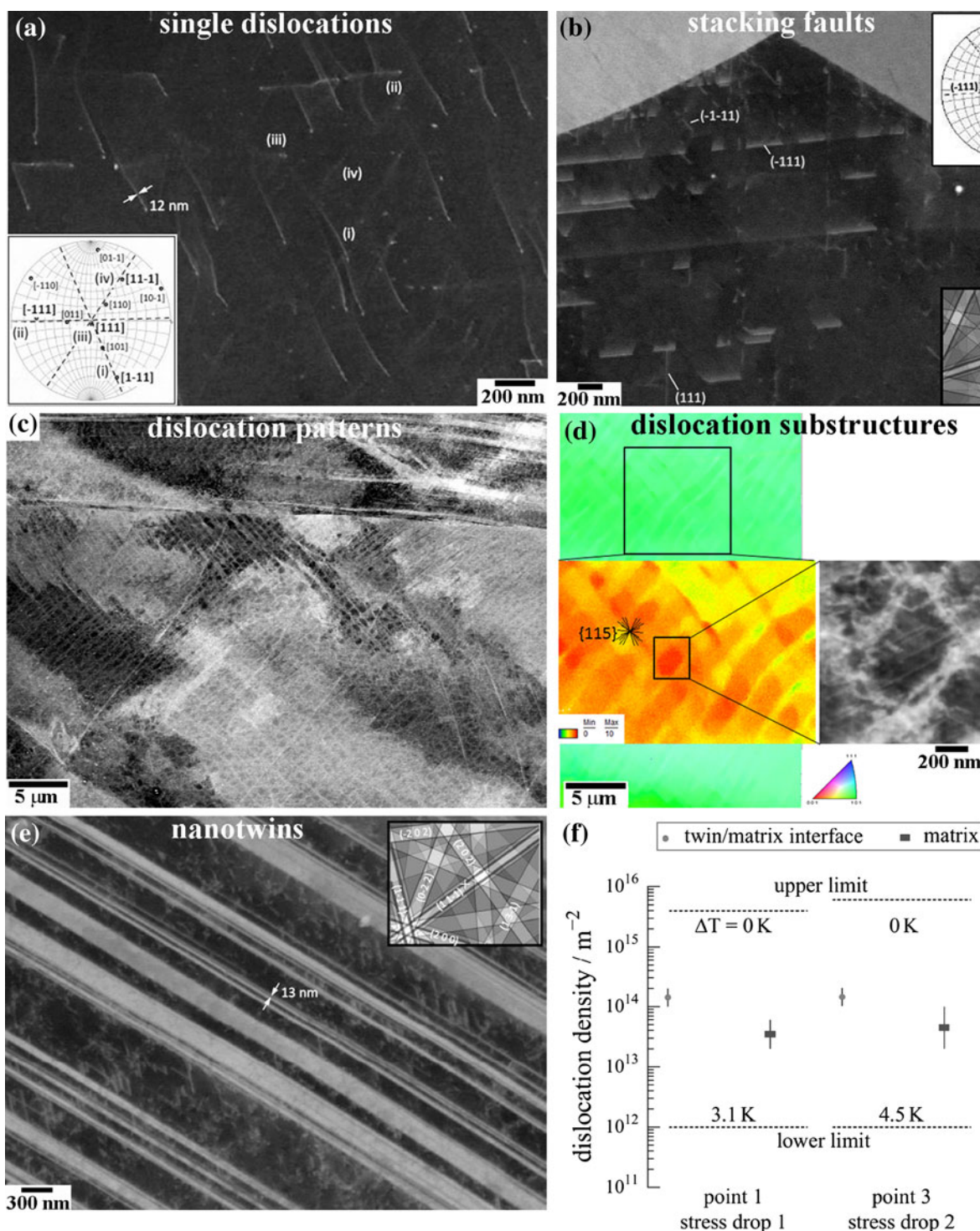


Fig. 3. Experimental application examples of the ECCI technique: (a) characterization of single dislocations, (b) stacking faults, (c–d) dislocation substructures, and (e) nanotwins; (f) measurement of dislocation densities (details can be found in Refs. 40, 41, 43).

are known. Under the present diffraction conditions and acceleration voltage, the probe depth is ~ 80 nm. Assuming that the visible dislocations intersect the sample surface and considering the corresponding projected dislocation lines, the inclination angles for the dislocation lines (i) and (ii) are

$\sim 10^\circ$ and 15° – 20° , respectively. These angles correspond to the inclination angles of the $[111]$ and $[\bar{1}\bar{1}\bar{1}]$ directions on the line traces (i) and (ii), respectively (Fig. 4b). The dislocations labeled as (iii) appear as small bright dots. These dislocations lie almost exactly perpendicular to the sample

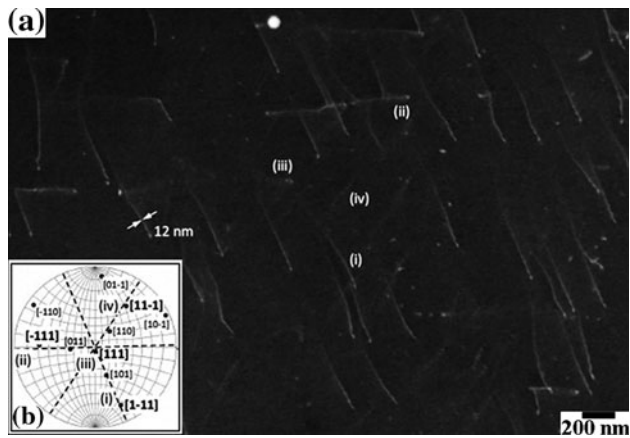


Fig. 4. (a): ECC image of dislocations taken after orienting the crystal into Bragg condition in a lightly deformed FeSi alloy.⁴³ (b): Stereographic projection of the orientation indicating the three $\langle 111 \rangle$ directions that correspond to line direction and Burgers vectors of the clearly visible dislocations.

surface and clearly correspond to screw dislocations with $[111]$ dislocation line directions and Burgers vectors. The dislocation lines (iv), although almost invisible, can be clearly attributed to $[1\bar{1}\bar{1}]$ line directions and Burgers vectors. As in ECCI, the $g \cdot b = 0$ invisibility criterion holds^{32,53} (g : diffraction vector, b : Burgers vector), and we can associate these dislocations with those fulfilling the invisibility criterion.

Measurement of Dislocation Densities

Average dislocation densities can be determined by counting the number of dislocations intersecting the observation area or using the relationship $\rho = 2N/Lt$, where N is the number of dislocation lines intersecting a grid of total line length L on the corresponding ECC image and t is the probe depth. The latter is a standard relationship used in TEM when individual dislocations can be clearly distinguished.^{3,54} The probe depth for imaging dislocations in ECCI has been estimated to be about $5\xi_g$ (calculations were performed using a dynamical diffraction approach by Wilkinson et al.²²). Figure 5 shows the average dislocation densities measured by ECCI in two to three grains of a Fe-3 wt.% Si alloy deformed to a macroscopic stress level of 500 MPa under two different diffraction conditions, namely, two-beam conditions with one set of hkl planes at Bragg orientation and three-beam conditions with two sets of hkl planes out-of-Bragg.⁴² The higher average density obtained by the second diffraction condition is ascribed to the larger number of excited reflectors, which provides, due to a channeling mechanism, a higher amount of visible dislocations. This figure also includes the average dislocation density determined by bright-field TEM in a sample deformed to the same macroscopic stress level. The average dislocation density was measured from TEM micrographs using the same

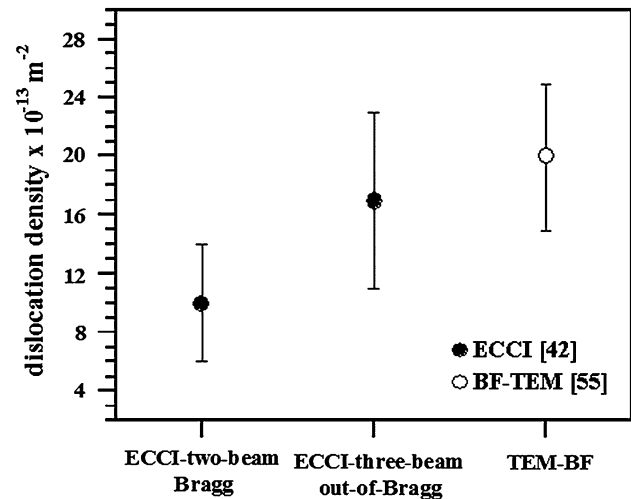


Fig. 5. Average dislocation densities determined in a Fe-3 wt.% Si alloy tensile deformed to a macroscopic stress of 500 MPa by two different electron microscopy techniques, namely, ECCI and TEM. Average dislocation densities were measured by ECCI under two different diffraction conditions: two-beam conditions with one set of hkl planes in the Bragg orientation and three-beam diffraction conditions with two sets of hkl planes out-of-Bragg (BF: bright field).

method as in the present work.⁵⁵ These findings reveal that the average dislocation density estimated from ECCI is in the same range as that determined from BF-TEM (BF: bright-field). In particular, the average dislocation density measured by ECCI in two-beam conditions is about two times smaller than that determined by BF-TEM. This result is well known from corresponding TEM-based estimates.³ Figure 5 also reveals that three-beam diffraction conditions with two sets of hkl planes out-of-Bragg provide a better estimation of the average dislocation density by ECCI, which is close to that obtained by bright-field TEM.

Characterization of Dislocation Substructures in Deformed Bulk Materials

The investigation of dislocation substructures has played an essential role in many topics in materials science in the last 50 years, such as strain hardening, polycrystal and crystal plasticity, internal stresses, and recrystallization. Due to the low misorientation of the dislocation boundaries involved (typically $<5^\circ$), its investigation has been mainly carried out by TEM. This has significantly limited the number of studies devoted to the quantitative characterization of dislocation patterns. In particular, this limitation has a pronounced influence on the understanding of polycrystal plasticity and strain hardening. According to dislocation mean free path-based theories of strain hardening, not only the dislocation pattern spacing must be evaluated but also its crystallographic orientation dependence with respect to the macroscopic stress as well.⁵⁶ We have recently explored the characteristics of the ECCI technique into the

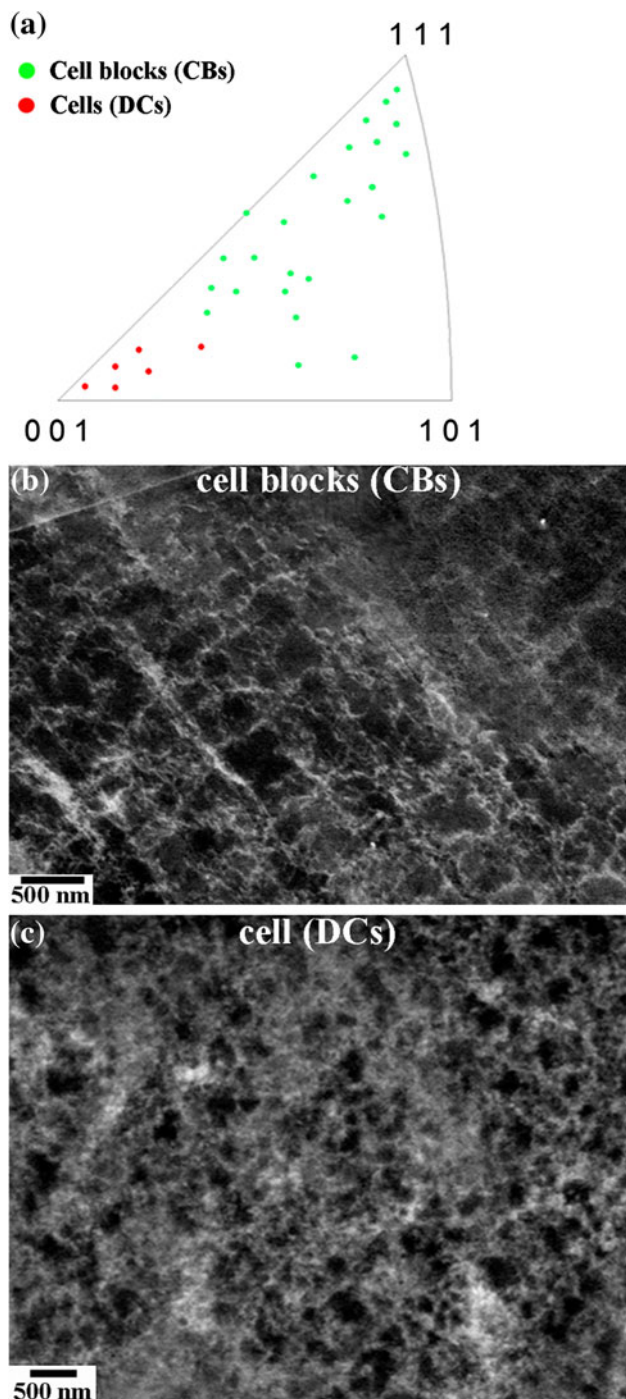


Fig. 6. (a): Inverse pole figure along the tensile axis direction showing experimental grain orientations of a Fe-30.5Mn-2.1Al-1.2C (wt.%) high-Mn steel tensile strained to 0.2 true strain/950 MPa (red dots: cells (DCs); green dots: cell blocks (CBs)), (b and c) ECCI images of (b) CBs and (c) DCs, respectively.³⁷

investigation of the evolution of dislocation substructures upon deformation in high-Mn steels.^{35–38,40} Dislocation configurations such as highly dense dislocation walls, cells, cell blocks, Taylor lattices, and microbands can be readily imaged and identified. Figure 6 shows an example of

the crystallographic orientation dependence of the dislocation substructure in a Fe-30.5Mn-2.1Al-1.2C (wt.%) high-Mn steel tensile strained to 0.2 true strain/950 MPa at an initial strain rate of $5 \times 10^{-4} \text{ s}^{-1}$.³⁷ Due to the wide field of view of the SEM, the evaluation of a large number of grains by ECCI is not as time consuming as in TEM. In this example, the crystallographic orientation dependence of the dislocation patterns, namely, cell blocks (CBs) and cells (DCs), was investigated in 30 individual grains with a representative orientation distribution that matches the overall crystallographic texture. Green and red dots correspond to CBs (green) and DCs (red), respectively. The data indicate that cell patterning has strong crystal orientation dependence. Equiaxed cells are only developed in grains oriented close to $\langle 001 \rangle // \text{TA}$ directions (Fig. 6c). The remaining analyzed grains contain a well-developed cell block structure (Fig. 6b). The shape of such structures depends on the number of active slip systems. The characterization of these dislocations provides new insights into the influence of alloying elements on the underlying dislocation mechanisms and, accordingly, into the strain hardening mechanisms.³⁷

CONCLUSIONS

The present article reviews the most relevant experimental and theoretical aspects associated with ECCI. The following conclusions can be drawn:

- The coupling of ECCI with EBSD provides an efficient and fast approach to perform ECCI of crystal defects, such as dislocations and stacking faults, under controlled diffraction conditions with enhanced contrast. From a technical point of view, the ECCI technique complements two of the main electron microscopy techniques, namely, EBSD and conventional diffraction-based TEM.
- We make use of a two-beam Bloch wave approach to interpret the channeling contrast associated with crystal defects. The approach captures the main features observed in the experimental contrast associated with stacking faults and dislocations.
- We provide several application examples of the EBSD-based ECCI approach on microstructure characterization, namely, characterization of single dislocations, measurement of dislocation densities, and characterization of dislocation substructures in deformed bulk materials.

ACKNOWLEDGEMENTS

The authors acknowledge the financial support by the German Research Foundation in the framework of SFB 761 “steel ab initio.” The authors also acknowledge intense discussions on the two-beam dynamical theory with Dr. A. Winkelmann (MPI Halle) and on the general application of ECCI with Prof. M. Crimp (Michigan State University).

REFERENCES

1. D.B. Williams and C.B. Carter, *Transmission Electron Microscopy. A Textbook for Materials Science* (New York: Springer, 2009).
2. G. Thomas and M.J. Goringe, *Transmission Electron Microscopy of Materials* (New York: Wiley, 1979).
3. P. Hirsch, A. Howie, R.B. Nicholson, D.W. Pashley, and M.J. Whelan, *Electron Microscopy of Thin Crystals* (Huntington: Robert E. Krieger, 1977).
4. J. Ayache, L. Beaunier, J. Boumendil, G. Ehret, and D. Laub, *Sample Preparation Handbook for Transmission Electron Microscopy* (New York: Springer, 2009).
5. H. Mughrabi, *Phil. Mag.* 23, 869 (1971).
6. T. Ungár, H. Mughrabi, and M. Wilkens, *Acta Metall.* 30, 1861 (1982).
7. T. Ungár, S. Ott, P.G. Sanders, A. Borbély, and J.R. Wertman, *Acta Mater.* 46, 3693 (1998).
8. B. Jakobsen, H.F. Poulsen, U. Lienert, and W. Pantleon, *Acta Mater.* 55, 3421 (2007).
9. B.C. Larson, W. Yang, G.E. Ice, J.D. Budai, and J.Z. Tischler, *Nature* 415, 887 (2002).
10. B. Jakobsen, H.F. Poulsen, U. Lienert, J. Almer, S.D. Shastri, H.O. Sørensen, C. Gundlach, and W. Pantleon, *Science* 312, 889 (2006).
11. A.J. Wilkinson, G. Meaden, and D.J. Dingley, *Ultramicroscopy* 106, 307 (2006).
12. W. Pantleon, *Scripta Mater.* 58, 994 (2008).
13. N. Zaafarani, D. Raabe, R.N. Singh, F. Roters, and S. Zaefferer, *Acta Mater.* 54, 1863 (2006).
14. E. Demir, D. Raabe, N. Zaafarani, and S. Zaefferer, *Acta Mater.* 57, 559 (2009).
15. D.P. Field, P.B. Trivedi, S.I. Wright, and M. Kumar, *Ultramicroscopy* 103, 33 (2005).
16. A.J. Wilkinson and P.B. Hirsch, *Micron* 28, 279 (1997).
17. D.C. Joy, D.E. Newbury, and D.L. Davidson, *Rev. Phys. Appl.* 53, 81 (1982).
18. E.M. Schulson, *J. Mater. Sci.* 12, 1071 (1977).
19. J.P. Spencer, C.J. Humphreys, and P.B. Hirsch, *Phil. Mag.* 26, 193 (1972).
20. D.G. Coates, *Phil. Mag.* 16, 1179 (1967).
21. J.T. Czernuszka, N.J. Long, E.D. Boyes, and P.B. Hirsch, *Phil. Mag. Lett.* 62, 227 (1990).
22. A.J. Wilkinson, G.R. Anstis, J.T. Czernuszka, N.J. Long, and P.B. Hirsch, *Phil. Mag A* 68, 59 (1993).
23. C. Trager-Cowan, F. Sweeney, P.W. Trimby, A.P. Day, A. Gholinia, N.H. Schmidt, P.J. Parbrook, A.J. Wilkinson, and I.M. Watson, *Phys. Rev. B* 75, 085301 (2007).
24. Y.N. Picard, M.E. Twigg, J.D. Caldwell, C.R. Eddy Jr, P.G. Neudeck, A.J. Trunek, and J.A. Powell, *Appl. Phys. Lett.* 90, 234101 (2007).
25. Y.N. Picard and M.E. Twigg, *J. Appl. Phys.* 104, 124906 (2008).
26. Y.N. Picard, M.E. Twigg, J.D. Caldwell, C.R. Eddy Jr, M.A. Mastro, and R.T. Holm, *Scripta Mater.* 61, 773 (2009).
27. C. van Essen, E.M. Schulson, and R.H. Donaghay, *J. Mater. Sci.* 6, 213 (1971).
28. C.G. van Essen, E.M. Schulson, and R.H. Donaghay, *Nature* 225, 847 (1970).
29. P. Morin, M. Pitaval, D. Besnard, and G. Fontaine, *Phil. Mag A* 40, 511 (1979).
30. M. Pitaval, P. Morin, J. Baudry, E. Viaria, and G. Fontaine, *Scan. Electron Microsc.* 1, 439 (1977).
31. M.A. Crimp, *Microsc. Res. Tech.* 69, 374 (2006).
32. M.A. Crimp, B.A. Simkin, and B.C. Ng, *Phil. Mag. Lett.* 81, 833 (2001).
33. I. Gutierrez-Urrutia, S. Zaefferer, and D. Raabe, *Scripta Mater.* 61, 737 (2009).
34. S. Zaefferer, *Ultramicroscopy* 107, 254 (2007).
35. I. Gutierrez-Urrutia and D. Raabe, *Acta Mater.* 59, 6449 (2011).
36. I. Gutierrez-Urrutia and D. Raabe, *Mater. Sci. For.* 702, 523 (2012).
37. I. Gutierrez-Urrutia and D. Raabe, *Acta Mater.* 60, 5791 (2012).
38. I. Gutierrez-Urrutia and D. Raabe, *Scripta Mater.* 68, 343 (2013).
39. D.R. Steinmetz, T. Jäpel, B. Wietbrock, P. Eisenlohr, I. Gutierrez-Urrutia, A. Saeed-Akbari, T. Hickel, F. Roters, and D. Raabe, *Acta Mater.* 61, 494 (2013).
40. I. Gutierrez-Urrutia and D. Raabe, *Scripta Mater.* 69, 53 (2013).
41. A. Eisenlohr, I. Gutierrez-Urrutia, and D. Raabe, *Acta Mater.* 60, 3994 (2012).
42. I. Gutierrez-Urrutia and D. Raabe, *Scripta Mater.* 66, 343 (2012).
43. S. Zaefferer and N.-N. Elhami, *Acta Mater.* (submitted).
44. A. Weidner, S. Martin, V. Klemm, U. Martin, and H. Biermann, *Scripta Mater.* 64, 513 (2011).
45. B.A. Simkin and M.A. Crimp, *Ultramicroscopy* 77, 65 (1999).
46. S. Zaefferer, *J. Appl. Cryst.* 33, 10 (2000).
47. W. Sigle, *Annu. Rev. Mater. Res.* 35, 239 (2005).
48. L. Reimer and H. Kohl, *Transmission Electron Microscopy. Physics of Image Formation* (New York: Springer, 2008).
49. D.C. Joy, *Monte Carlo Modeling for Electron Microscopy and Microanalysis* (Oxford: Oxford University Press, 1995).
50. M.E. Twigg and Y.N. Picard, *J. Appl. Phys.* 105, 093520 (2009).
51. S.L. Dudarev, P. Rez, and M.J. Whelan, *Phys. Rev. B* 51, 3397 (1995).
52. A. Winkelmann, B. Schroeter, and W. Richter, *Ultramicroscopy* 98, 1 (2003).
53. A.J. Wilkinson and P.B. Hirsch, *Phil. Mag. A* 72, 81 (1995).
54. R.K. Ham, *Phil. Mag.* 69, 1183 (1961).
55. D. Griffiths and J.N. Riley, *Acta Metall.* 14, 755 (1966).
56. D. Kuhlmann-Wilsdorf, *Dislocations in Solids*. vol. 11, eds. F.R.N. Nabarro and M.S. Duesbery (2002).